Nano Research

Open Access

Research Article

Plasmon-induced local electric field improved hydrogen evolution reaction on Ag/Mo_2C nanosheets

HuangJingWei Li[1,§], Xin Zi[1,§], Jun Wu[2,§], Xinli Wang[3], Li Zhu[4], Qiyou Wang[1], Jianfu Han[5], Junwei Fu[1], Hongmei Li[1], Kai Huang[5], Yu Chen[1], and Min Liu[1] ✉

[1] *School of Physics, State Key Laboratory of Powder Metallurgy, Hunan Joint International Research Center for Carbon Dioxide Resource Utilization, Central South University, Changsha 410083, China*
[2] *School of Metallurgy and Environment, Central South University, Changsha 410083, China*
[3] *Institute of High Energy Physics, Chinese Academy of Sciences (CAS), Beijing 100049, China*
[4] *Nano-Institute Munich, Faculty of Physics, Ludwig-Maxilimians-Universität München, München 80539, Germany*
[5] *Hunan Institute of Advanced Sensing and Information Technology, Xiangtan University, Xiangtan 411105, China*
§ *HuangJingWei Li, Xin Zi, and Jun Wu contributed equally to this work.*

Cite this article: *Nano Research*, **2025**, *18*, 94907146. https://doi.org/10.26599/NR.2025.94907146

ABSTRACT: Electrocatalytic water splitting offers a promising way for hydrogen production with near-zero emissions. Carbides, such as molybdenum carbides (Mo_2C), are promising materials for hydrogen evolution reaction (HER) but still suffer from poor intrinsic water activation properties. Here, we developed a plasmon-induced local electric field (PILEF) strategy to solve this barrier. Silver (Ag) nanoparticles decorated Mo_2C nanosheets (Ag/Mo_2C) were successfully prepared by electrostatic adsorption. The visible light excited the PILEF on Ag/Mo_2C remarkably reducing the activation energy by 92.7 kJ·mol^{-1} from 147.3 kJ·mol^{-1} of Mo_2C to 54.6 kJ·mol^{-1}. As a result, the plasmonic Ag/Mo_2C significantly enhances ~ 2.3-fold of the current density from 2.8 mA·cm^{-2} of Mo_2C to 6.5 mA·cm^{-2} at −3 V vs. RHE and reduces the overpotential by 104 mV from 403 mV of dark state to 299 mV of light state at the current density of 10 mA·cm^{-2}, achieving better performance than reported catalysts. This research demonstrates that PILEF enhances HER activities, offering a potential strategy for boosting the intrinsic activities of catalysts.

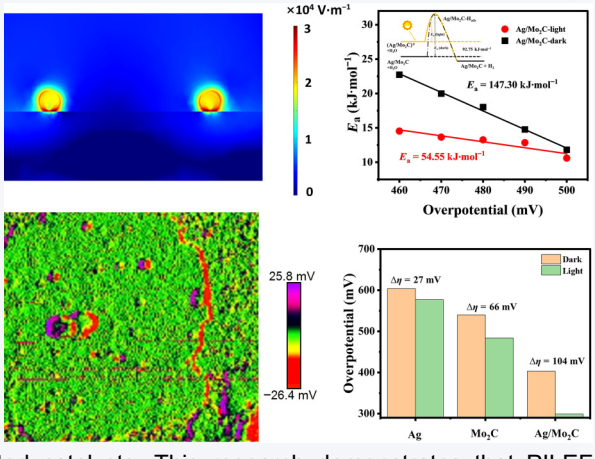

KEYWORDS: sliver particles, plasmon effect, field effect, hydrogen evolution reaction (HER), electrocatalysis

1 Introduction

Hydrogen (H_2) is a clean and renewable energy with high mass-to-energy density and zero emissions [1–4]. Electrocatalytic water splitting has been recognized as an efficient and promising method for H_2 production [5–7]. To date, hydrogen evolution reaction (HER) can be easily achieved by precious metals [8–12], such as Pt and Ru. However, the scarcity and high cost of these precious metals have seriously hampered their practical utilization. There is a need to seek a non-precious metal catalyst instead.

Theoretical and experimental studies have shown that the non-precious metal catalyst molybdenum carbide (Mo_2C) is a promising catalyst for HER, which has high electrical conductivity and excellent hydrogen adsorption energy due to the electronic structure similar to Pt group elements [13–16]. The Mo_2C is also a two-dimensional nanosheet, which facilitates the loading of other nanomaterials. However, the HER activities of Mo_2C have not reached the expected performance close to Pt [17–19]. To address this issue, element doping or material hybridization has been used to improve the catalytic activity of Mo_2C, which can modify their band structure and create additional active sites [20–26]. However, these routes are still not able to alter Mo_2C's poor intrinsic water activation nature, resulting in high demand to find suitable energy implantation ways to conquer this barrier.

Plasmonic metals (such as Au, Ag, and Cu) can absorb external solar energy to improve the catalytic performance through the plasmonic effect. Especially, the plasmonic metal can generate a

Received: November 6, 2023; **Revised:** January 15, 2024
Accepted: January 15, 2024

✉Address correspondence to minliu@csu.edu.cn

localized electric field around the metal surface [27–37], which accelerates the electrochemical processes. Moreover, the excited hot electrons can reduce the reaction energy barriers [38–40]. Ag has been used as a photocatalytic enhancer due to their excellent plasmonic effect in the visible region [34, 41, 42]. For example, hot electrons excited from Ag nanocubes increase the carrier density and the surface-exposed Ag (111) crystalline surface is more conducive to hydrogen desorption [43, 44]. Additionally, Ag can absorb photons and excite the conduction electrons in the 5sp orbitals to higher-energy states [45]. These excited electrons can participate in and expedite chemical reactions.

Here, plasmonic Ag/Mo_2C nanosheets were successfully constructed by electrostatic adsorb for excellent HER. Finite element method (FEM) simulation revealed the enhancement of plasmon-induced local electric field (PILEF) and the excitation of hot electrons at the contact interface of Ag and Mo_2C. First-principles calculations uncover the interfacial charge transfer process and the effect of the electric field on the adsorption of intermediates. Kelvin probe force microscopy (KPFM) measurements confirmed the high electric field around the Ag surface. Arrhenius equation analyses presented a significant reduction in the activation energy of the Ag/Mo_2C (ΔE_a) of 92.7 kJ·mol^{-1} under illumination. As a result, a significant reduction in overpotential ($\Delta\eta$) of 104 mV at the current density of 10 mA·cm^{-2} and a Tafel slope as low as 58 mV·dec^{-1} were achieved on Ag/Mo_2C nanosheets. This work examines the cooperative interaction between Ag and Mo_2C, emphasizing the potential of the plasmonic effect to promote electrocatalysis.

2 Experimental

2.1 COMSOL multiphysics simulations

The substrate was defined as a layer of Mo_2C, the hemisphere Ag particles located on the surface and surrounded by water. The plane waves incident along the backward direction of the *Z*-axis. The perfectly matched layers were defined to embrace physical domains to absorb all the scattered waves. The variate was defined as the wavelength of the excitation wave and the radius of the Ag particles. The background field was first computed, and then the total field and power loss were accomplished when the nanoparticle was introduced.

2.2 Density functional theory (DFT) calculations

All DFT calculations for periodic material systems were performed with the Vienna *ab initio* simulation package (VASP) using the projector-augmented wave (PAW) method [46, 47]. The exchange–correlation function was handled using the generalized gradient approximation (GGA) formulated by the Perdew–Burke–Ernzerhof (PBE) [48]. The van der Waals (vdW) interactions are described with the DFT-D3 method in Grimme's scheme [49]. The interaction between the atomic core and electrons was described by the projector augmented wave method [50–52]. The plane-wave basis set energy cutoff was set to 500 eV. The Brillouin zone was sampled with a 3 × 3 × 1 grid centered at the gamma (Γ) point for geometry relaxation. All the slabbed models possessed a vacuum spacing of ≈ 15 Å sampled, ensuring negligible lateral interaction of adsorbates. The bottom layers about half of the structure were kept frozen at the lattice position. All structures with a dynamic magnetic moment were fully relaxed to optimize without any restriction until their total energies were converged to $< 1 \times 10^{-6}$ eV, and the average residual forces were < 0.02 eV·Å^{-1}.

2.3 Materials

MoO_3 (99.9%), $K_2HPO_4{\cdot}3H_2O$ (99.99%), $KH_2PO_4{\cdot}3H_2O$ (99.99%), glucose, $NaBH_4$, $AgNO_3$, and trisodium citrate were purchased from Alfa Aesar. All chemicals were used in this study without further purification. Ar–H_2 (10% H_2), and N_2 (99.999%) were purchased from Hunan Mande Gas Co. LTD.

2.4 Prepare of Ag/Mo_2C

Ag nanoparticles: An aqueous solution of $NaBH_4$ (6 mL, 10 mM) was added to a 200 mL solution of $AgNO_3$ (0.25 mM) and trisodium citrate (0.25 mM). The reaction was stirred for 30 min, resulting in a yellow colloidal silver solution, and was then left undisturbed overnight to obtain the Ag nanoparticles [31, 32]. The size of Ag nanoparticles is about 15 nm. The different size Ag nanoparticles can be adjusted by the amount of the $NaBH_4$. We use 3 and 24 mL $NaBH_4$ (10 mM) obtained ~ 10 and ~ 40 nm Ag nanoparticles, respectively.

Mo_2C nanosheets (NSs): The setup is a typical CVD system, which constitutes a clean quartz tube and tube furnace. First, MoO_2 NSs were grown on the quartz tube tail by a chemical vapor reduction process using commercial MoO_3 powders (0.5 g). The reaction was performed in the presence of mixed Ar–H_2 (10% H_2) gases (200 sccm) at 900 °C for 60 min, and the purple MoO_2 NSs were collected at the tail end of the quartz tube. Second, commercial glucose powders (1 g) were mixed with 100 mg of obtained MoO_2 NSs, which were placed in the tube furnace with Ar–H_2 gas to remove air. The mixture was calcined at 450 °C for 2 h and then 700 °C for 2 h to form Mo_2C NSs.

Ag/Mo_2C nanosheets: Self-assembly of Mo_2C NSs with Ag nanoparticles. Mo_2C NSs were assembled with Ag nanoparticles through the electrostatic interaction. Mo_2C NSs (10 mg) were dispersed in 10 mL of ethanol under vigorous stirring. Then, 10 mL of the as-prepared Ag solution was added dropwise. After stirring for 1 h, the resulting sample (denoted as Ag/Mo_2C) was collected and washed with water.

2.5 Characterizations

X-ray diffraction (XRD) was characterized by Rigaku Miniflex 600. X-ray photoelectron spectroscopy (XPS) measurements were performed on a Thermo Fisher ESCALAB 250Xi spectrometer using monochromatized Al Kα excitation. The morphology was imaged by a field emission scanning electron microscope (FESEM, Regulus8100, Hitachi) and a transmission electron microscope (TEM, JEM-2100F, JEOL). The thickness of samples was measured by Atomic force microscopy (AFM, Dimension Icon, Bruker), and the surface potential was measured by Kelvin probe force microscope (KPFM) mode on the n-type silicon wafer, which was irradiated by light through the Perfect light instrument.

2.6 Electrochemical measurements

The electrochemical measurements were first performed using a 3 mm glassy carbon in a three-electrode system. The data were collected by using a Princeton electrochemical workstation. The GC, carbon rod, and Ag/AgCl/saturated KCl were used as working, counter, and reference electrodes, respectively. The catalyst inks were prepared by dispersing catalysts (5 mg) into a dispersant composed of 40 μL 5 wt.% Nafion solution and 1 mL mixed

solution of ethanol/water (v/v = 1/1) with the assistance of sonication for 30 min. 10 μL of the catalyst ink was loaded onto a rotating disk electrode (RDE) (catalyst loading is 0.25 mg·cm^{-2}). Linear sweep voltammetry (LSV) of HER was performed in 0.5 M phosphoric acid buffer solution (PBS) at a scan rate of 2 mV·s^{-1}. All polarization curves were recorded manually *iR*-corrected and converted to the reversible hydrogen electrode (RHE) scale. All tests were carried out in 0.5 M PBS solution and potential was referred versus RHE by $E_{RHE} = E_{Ag/AgCl} + 0.197 + 0.0591 \times pH$. The solution was bubbled by N_2 gas for 20 min before the HER. The electrochemical impedance spectra of the fabricated electrodes under the frequency range from 100 kHz to 0.1 Hz at 100 mV overpotential versus RHE.

3 Results and discussion

To explore the PILEF strength and distribution on Ag surfaces, FEM simulations were adopted. We simulated the Ag nanoparticles with different sizes that affect the intensity of the electric field (Fig. S1 in the Electronic Supplementary Material (ESM)). As the size decreases, the surface electric field intensity increases. At the contact surface between 15 nm Ag and Mo_2C, there is a significantly enhanced local electric field with an intensity of 3.1×10^4 V·m^{-1} compared to Mo_2C (Fig. 1(a)). In addition, the electron density is also much enhanced at the contact surface as can be seen from the electron distribution (Figs. S1(b) and S1(d) in the ESM). These results show that the Ag surface has a strong PILEF and more excited electrons under illumination. To gain more understanding of the electric field for the HER, we performed first-principles calculations. In Fig. 1(b), after adsorbing H atom, 0.001 electron is transferred to the H atom at an electric field of −0.5 V·Å^{-1}. The uneven charge distribution on the H atoms favors the activation and adsorption of H atom. In contrast, no apparent electron transfer occurs between the catalyst and H atom without an electric field. Moreover, there is a 0.2 electron transfer from Ag to Mo_2C, which weakens the adsorption of *H (Fig. 1(c) and Fig. S2 in the ESM). Thus overall, as shown in Fig. 1(d), Ag/Mo_2C exhibits an optimal adsorption free energy (0.24 eV), compared to Ag (−2.02 eV) and Mo_2C (−0.61 eV).

Motivated by theoretical analyses, Ag/Mo_2C nanosheets were synthesized by a simple method with solution reduction and electrostatic assembly (Fig. 2(a)). Zeta potentials of Ag and Mo_2C measured in an aqueous solution were +40.2 and −60.8 mV, respectively, indicating they had close contact with each other via electrostatic interaction (Fig. S3 in the ESM). TEM and scanning electron microscopy (SEM) images showed the Ag nanoparticles with ~ 15 nm were randomly decorated on the surfaces of Mo_2C (Fig. 2(b) and Figs. S4 and S5 in the ESM). The lattice fringe of 0.26 nm in the high-resolution TEM (HRTEM) image (Fig. 2(c)) corresponded to the (111) crystal plane of Mo_2C, and the 0.23 nm could be assigned to the (111) plane of Ag [43]. Elemental mapping images showed that Ag, Mo, and C were uniformly distributed (Fig. 2(d)).

To obtain more structural information, XRD and XPS measurements were performed. The XRD peaks at 38.2° and 44.1° are the (100) and (111) crystal faces of Ag (PDF #040783) and the peak at 39.8° is the (100) crystal face of Mo_2C (PDF #350787), indicating the incorporation of Ag on Mo_2C (Fig. 3(a)) [53, 54]. XPS spectra showed that the binding energies of Ag $3d_{3/2}$ and Ag $3d_{5/2}$ in Ag/Mo_2C were positively shifted by approximately 0.28 eV and 0.32 eV, respectively, as compared to those in metallic Ag (Fig. 3(b)). In contrast, Mo 3d XPS spectra of Mo^{5+} and Mo^{6+} exhibited a negative shift in Ag/Mo_2C compared to those of Mo_2C, indicating

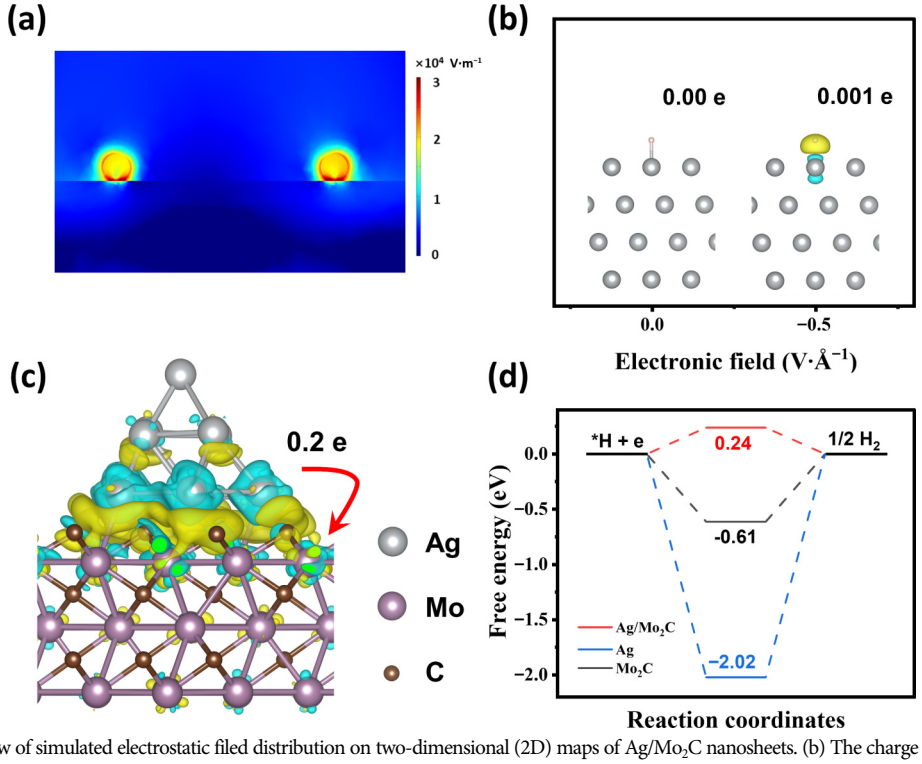

Figure 1 (a) The side view of simulated electrostatic filed distribution on two-dimensional (2D) maps of Ag/Mo_2C nanosheets. (b) The charge density difference between adsorbing H atom and Ag with/without electric fields, including the amount of election transferred from catalyst to H atom. The abscissa shows with/without electric fields. (c) The charge density difference and Bader charge transfer at the interface of Ag/Mo_2C. Yellow and blue regions indicate electron accumulation and depletion, respectively. (d) The Gibbs free energy of H* adsorption on Ag/Mo_2C, Ag, and Mo_2C.

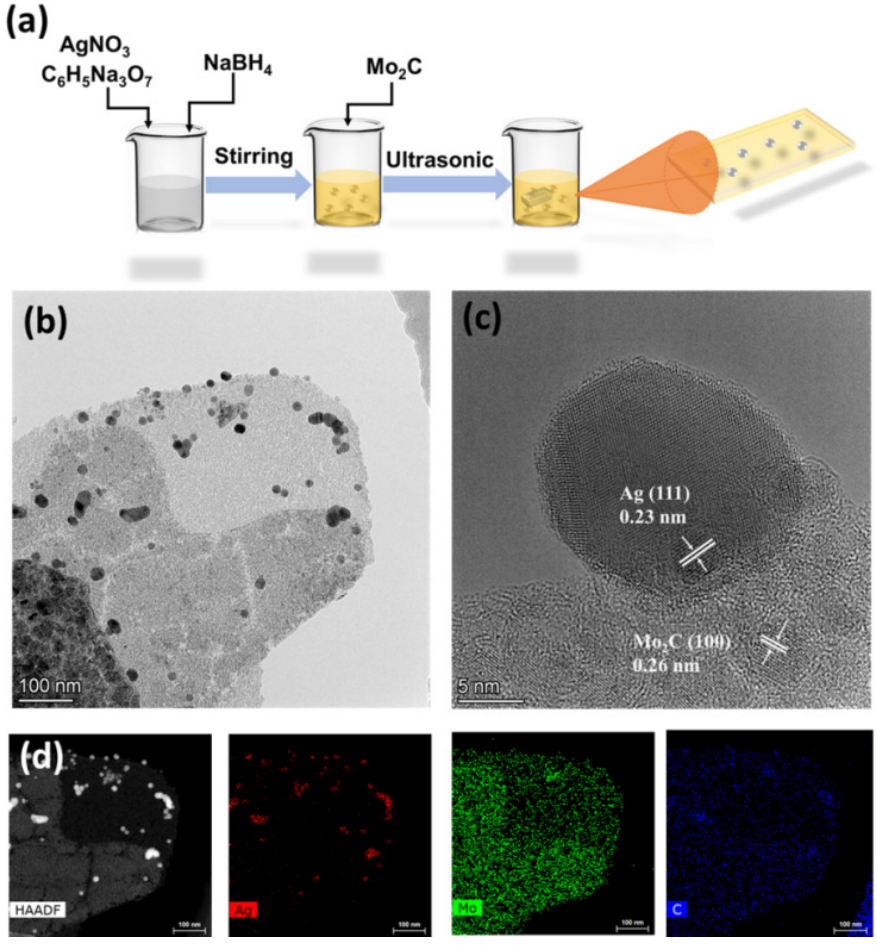

Figure 2 (a) The schematic diagram of material synthesis. (b) The TEM and (c) HRTEM images of Ag/Mo_2C. (d) Ag, Mo, C element mapping of Ag/Mo_2C.

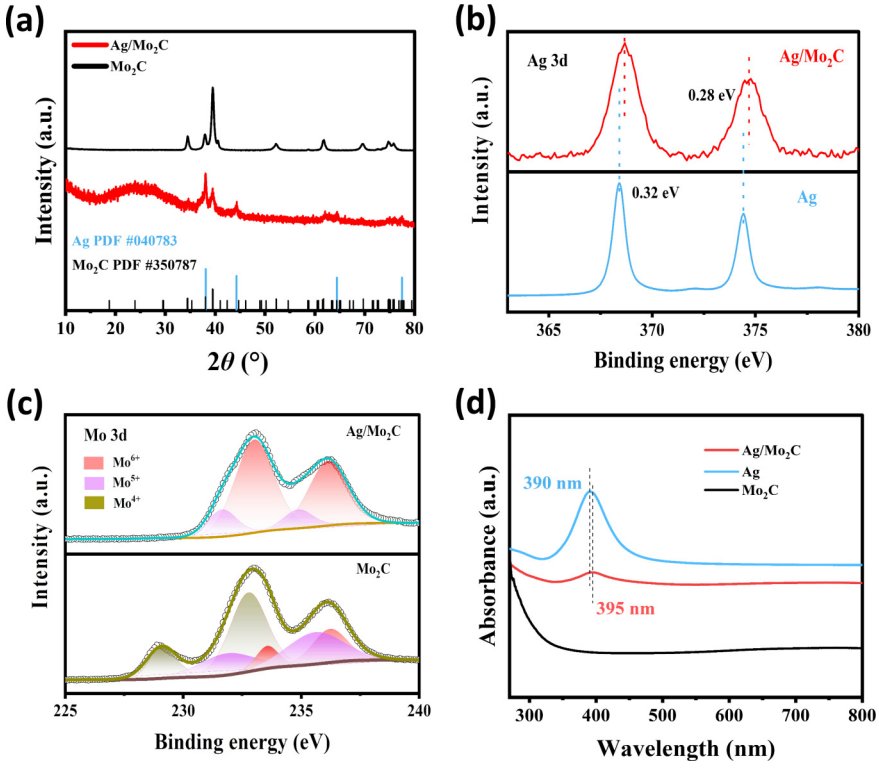

Figure 3 (a) The XRD patterns of Ag/Mo_2C and Mo_2C. (b) The Ag 3d of Ag/Mo_2C and Ag. (c) Mo 3d XPS spectra of Ag/Mo_2C and Mo_2C. (d) UV–Vis absorption spectra of Ag, Mo_2C, and Ag/Mo_2C.

that Mo is an electron-acceptor (Fig. 3(c)). These results demonstrated the electron transfer from Ag to Mo_2C in Ag/Mo_2C. To detect the surface plasmon excitation of Ag/Mo_2C, ultraviolet–visible (UV–Vis) tests were carried out. The Ag/Mo_2C showed an intense light absorption peak centered at 395 nm, which can be assigned to the surface plasmon excitation of Ag [55]. Notably, there is an approximately 5 nm red shift in Ag/Mo_2C compared with that of metallic Ag, proving electronic transfer between Ag and Mo_2C (Fig. 4(d)). To gain deeper insights into electron transfer from an energy band aspect. The energy band structure of Mo_2C is derived from Mott–Schottky plots (Fig. S6 in the ESM) and previous literature [54]. The flat potential is determined to be 0.34 (vs. NHE) in the dark which reduces to 0.22 V (vs. NHE) under the illuminiation. The Fermi level of Mo_2C in the light is raised to an energy level closer to the redox pair H_2O/H_2 redox potential (0 V) (Fig. S6(c) in the ESM), which would reduce the overpotential of Mo_2C [28, 39].

To accurately determine the PILEF intensity, we employed the KPFM to assess the contact potential difference (CPD) at the interfacial regions. As depicted in Fig. 4(a), we found that Ag was uniformly distributed on the Mo_2C nanosheets. It can be seen that a high CPD of 16 mV around Ag under the illumination, was 3 mV higher than that of the Mo_2C substrate (Fig. 4(b)). To gain more evidence for the plasmon-induced local electric field enhanced HER activity of Ag/Mo_2C, the activation energies (E_a) of HER with light and dark were further performed to provide quantitative insights into the energetics (Fig. 4(c) and Fig. S7 in the ESM). As shown in Fig. 4(d), the E_a of 147.3 kJ·mol^{-1} for Ag/Mo_2C under dark could be decreased to 54.6 kJ·mol^{-1} under illumination, a reaction activation energy decrease of 92.7 kJ·mol^{-1} resulted from the Ag plasmonic activation under the illumination (Fig. 4(d) inset). This result leads to an increase in the energy level of Mo_2C favoring the HER.

To evaluate the water splitting performance, the HER activity of the samples in 0.5 M PBS electrolyte using a standard three-electrode system. The linear scanning voltage (LSV) showed that all catalysts exhibited weak HER activity in the dark (Fig. 5(a)). The activity of Ag/Mo_2C was relatively better with an overpotential of 403 mV at the current density of 10 mA·cm^{-2}. Notably, the overpotential of Ag/Mo_2C exhibited a significant decrease of 104 mV at 10 mA·cm^{-2} under light illumination, while exerting subtle effects on both Ag and Mo_2C. (Fig. 5(b)). As shown in Fig. S8 in the ESM, CV curves at different sweep speeds were tested to obtain the double-layer capacitance (C_{dl}) values of the catalysts. The value of the C_{dl} can reflect the electrochemical active surface area (ECSA). From Fig. S8(d) in the ESM, Ag/Mo_2C (0.58 mF·cm^{-2}) showed the most ECSA compared with that of the Mo_2C (0.53 mF·cm^{-2}) and Ag (0.24 mF·cm^{-2}) electrocatalysts, which confirmed the excellent HER performance. To identify the real activity, the current density was normalized by ECSA. The Ag/Mo_2C still has the lowest overpotential in the normalized in Fig. S9 in the ESM. Furthermore, to identify the different sizes of Ag nanoparticles affect the activity. We also synthesized the Ag nanoparticles of 10 and 40 nm (Fig. S10 in the ESM). The original 15 nm Ag nanoparticles have the optimal catalytic activity (Fig. S11 in the ESM).

As shown in Fig. 5(c), the Tafel slope of Ag/Mo_2C exhibited a sharp decrease to 58 mV·dec^{-1}, significantly smaller than the value measured in the dark (170 mV·dec^{-1}). This suggests that the HER mechanism shifts from the Volmer step to the Heyrovsky step with the PILEF. The Ag/Mo_2C electrodes displayed the largest current density difference (Δj = 6.5 mA·cm^{-2}) compared to those of Mo_2C (2.8 mA·cm^{-2}) and Ag (0.23 mA·cm^{-2}) at −0.3 V vs. RHE under light irradiation (Fig. 5(d)). The Ag/Mo_2C exhibited an approximately 2.3-fold increase in current density compared to Mo_2C, which is even better than those of reported catalysts (Table S1 in the ESM). This indicates that the local electronic field excited from Ag under illumination enhances the lifetime of

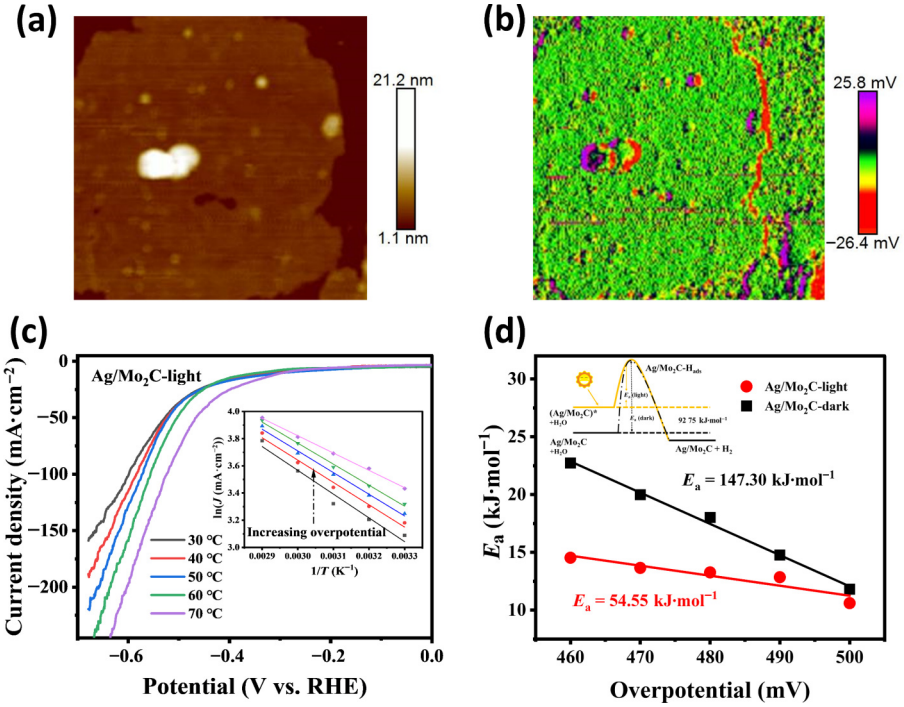

Figure 4 (a) The AFM topography of total Ag/Mo_2C nanosheets. (b) The detailed topography and surface potential image of Ag/Mo_2C. (c) HER activity of Ag/Mo_2C under light at different temperatures (inset: Arrhenius plots). (d) Activity energy with the light on and off at the zero overpotential is obtained through trend extrapolation (inset: Schematic representation of the activity energy change of Ag/Mo_2C by light irradiation).

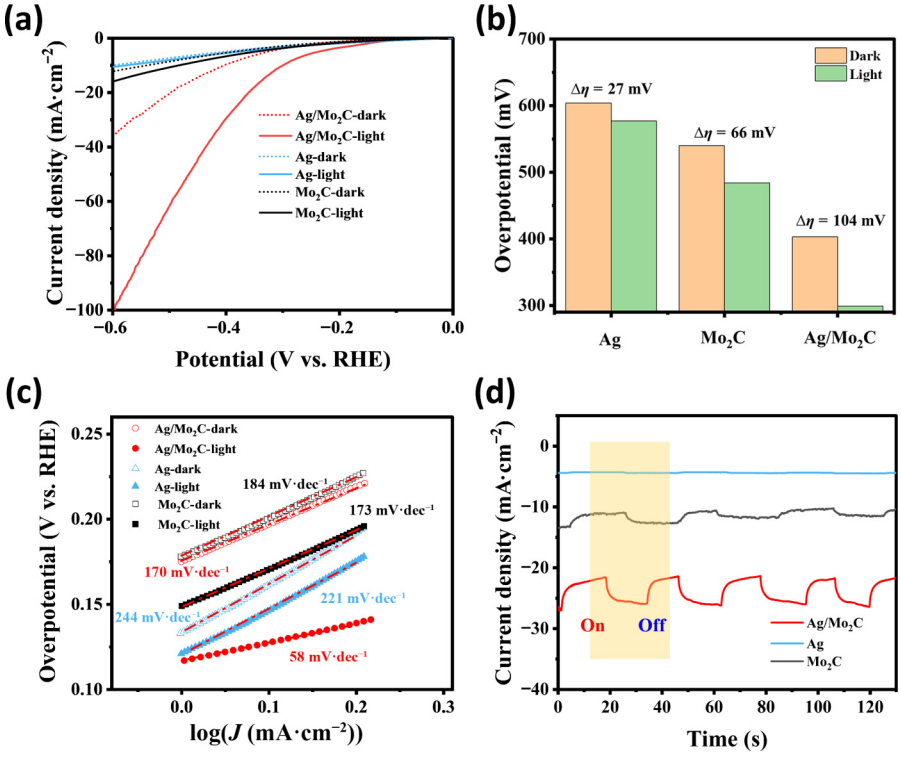

Figure 5 (a) HER polarization curves. (b) Overpotential of Ag, Mo_2C, and Ag/Mo_2C. (c) The Tafel slopes of Ag, Mo_2C, and Ag/Mo_2C in the absence or presence of light irradiation. (d) *I*–*t* curves at the potential of −0.3 V vs. RHE.

photogenerated carriers and provides more electrons for catalytic reactions. The impedance spectrum analyses demonstrated that the impedance of Ag (648 Ω), Mo_2C (47 Ω), and Ag/Mo_2C (22 Ω) were linearly decreased (Fig. S12 in the ESM). Furthermore, upon turning on the light, the impedance of Ag/Mo_2C decreases from 22 to 14 Ω, indicating that the local electric field is generated around the surface of Ag, facilitating charge transport to the Mo_2C.

4 Conclusions

In summary, we used the FEM simulation to explore the surface of Ag has a high PILEF under illumination, which benefits the excited electrons to participate in the reaction. Then the Ag/Mo_2C were successfully synthesized by solution reduction and electrostatic assembly, which was confirmed by TEM and spectroscopic characterization. KPFM experiments showed that a local electric field is excited around the surface of Ag, reducing the E_a of the Ag/Mo_2C by 92.7 kJ·mol^{-1} under illumination. As a result, we found the HER overpotential of the Ag/Mo_2C was reduced by 104 mV compared to Mo_2C at the current density of 10 mA·cm^{-2} and the current density of Ag/Mo_2C was enhanced ~ 2.3 fold compared to Mo_2C. Our work demonstrated the PILEF from plasmonic metals can effectively improve the activity of electrolysis reactions.

Electronic Supplementary Material: Supplementary material (further details of the COMSOL simulation with differernt size Ag, DFT calculations, zeta potential, SEM measurements, TEM imaging, Mott–Schottky test, activity energy, ECSA, normalized LSV, LSV with differernt size Ag, and EIS measurements) is available in the online version of this article at https://doi.org/10.26599/NR.2025.94907146.

Data availability

All data needed to support the conclusions in the paper are presented in the manuscript and the Electronic Supplementary Material. Additional data related to this paper may be requested from the corresponding author upon request.

Acknowledgements

We thank the China Postdoctoral Science Foundation (Nos. 2023M731175 and GZB20230232), the National Natural Science Foundation of China (Nos. 22376222, 52372253, 22002189, and 52202125), the Science and Technology lnnovation Program of Hunan Province (No. 2023RC1012), the National Science Foundation of Hunan Province (No. 2021JJ30864), Central South University Research Programme of Advanced Interdisciplinary Studies (No. 2023QYJC012), Central South University Innovation-Driven Research Programme (No. 2023CXQD042). The authors thanks Hengyue Xu for the help of DFT calculations. Project supported by State Key Laboratory of Powder Metallurgy, Central South University, Changsha, China. We are grateful for resources from the High Performance Computing Center of Central South University.

Declaration of competing interest

All the contributing authors report no conflict of interest in this work.

Author contributions

H. J. W. L.: Conceptualization, investigation, data curation, formal analysis, writing – original draft. X. Z.: Investigation, data curation.

J. W.: Formal analysis, writing – original draft. X. L. W.: Methodology, data curation. L. Z.: Validation, formal analysis. Q. Y. W.: Validation, formal analysis. J. F. H.: Data curation. J. W. F.: Validation, formal analysis. H. M. L.: Validation, formal analysis. K. H.: Data curation, formal analysis. Y. C.: Resources, formal analysis. M. L.: Conceptualization, resources, writing – review & editing, supervision, funding acquisition. All the authors have approved the final manuscript.

Use of AI statement

None.

References

[1] Shang, B.; Cui, X. Q.; Jiao, L.; Qi, K.; Wang, Y. W.; Fan, J. C.; Yue, Y. Y.; Wang, H. Y.; Bao, Q. L.; Fan, X. F. et al. Lattice-mismatch-induced ultrastable 1T-phase MoS_2–Pd/Au for Plasmon-enhanced hydrogen evolution. *Nano Lett.* **2019**, *19*, 2758–2764.

[2] Jiang, W. Y.; Wu, X. X.; Chang, J. Q.; Ma, Y. H.; Song, L. T.; Chen, Z. X.; Liang, C.; Liu, X. F.; Zhang, Y. Integrated hetero-nanoelectrodes for Plasmon-enhanced electrocatalysis of hydrogen evolution. *Nano Res.* **2021**, *14*, 1195–1201.

[3] Zhang, Y. Z.; Du, J.; Luo, R. C.; Wang, Z. Q.; Wang, Z. L.; Han, J. H.; Liu, P.; Fujita, T.; Xue, Q. K.; Chen, M. W. 3D bicontinuous nanoporous plasmonic heterostructure for enhanced hydrogen evolution reaction under visible light. *Nano Energy* **2019**, *58*, 552–559.

[4] Wang, X. T.; Liow, C.; Qi, D. P.; Zhu, B. W.; Leow, W. R.; Wang, H.; Xue, C.; Chen, X. D.; Li, S. Z. Programmable photo-electrochemical hydrogen evolution based on multi-segmented CdS–Au nanorod arrays. *Adv. Mater.* **2014**, *26*, 3506–3512.

[5] Jiao, Y.; Zheng, Y.; Jaroniec, M.; Qiao, S. Z. Design of electrocatalysts for oxygen-and hydrogen-involving energy conversion reactions. *Chem. Soc. Rev.* **2015**, *44*, 2060–2086.

[6] Jiao, S. L.; Fu, X. W.; Wang, S. Y.; Zhao, Y. Perfecting electrocatalysts via imperfections: Towards the large-scale deployment of water electrolysis technology. *Energy Environ. Sci.* **2021**, *14*, 1722–1770.

[7] Wu, H.; Huang, Q. X.; Shi, Y. Y.; Chang, J. W.; Lu, S. Y. Electrocatalytic water splitting: Mechanism and electrocatalyst design. *Nano Res.* **2023**, *16*, 9142–9157.

[8] Li, H. J. W.; Liu, K.; Fu, J. W.; Chen, K. J.; Yang, K. X.; Lin, Y. Y.; Yang, B. P.; Wang, Q. Y.; Pan, H.; Cai, Z. J. et al. Paired Ru–O–Mo ensemble for efficient and stable alkaline hydrogen evolution reaction. *Nano Energy* **2021**, *82*, 105767.

[9] Shan, J. Q.; Ling, T.; Davey, K.; Zheng, Y.; Qiao, S. Z. Transition-metal-doped RuIr bifunctional nanocrystals for overall water splitting in acidic environments. *Adv. Mater.* **2019**, *31*, 1900510.

[10] Chen, W.; Wu, B. B.; Wang, Y. Y.; Zhou, W.; Li, Y. Y.; Liu, T. Y.; Xie, C.; Xu, L. T.; Du, S. Q.; Song, M. L. et al. Deciphering the alternating synergy between interlayer Pt single-atom and NiFe layered double hydroxide for overall water splitting. *Energy Environ. Sci.* **2021**, *14*, 6428–6440.

[11] Wen, Q. J.; Yang, K.; Huang, D. J.; Cheng, G.; Ai, X. M.; Liu, Y. M.; Fang, J. K.; Li, H. Q.; Yu, L.; Zhai, T. Y. Schottky heterojunction nanosheet array achieving high-current-density oxygen evolution for industrial water splitting electrolyzers. *Adv. Energy Mater.* **2021**, *11*, 2102353.

[12] Wen, Q. L.; Duan, J. Y.; Wang, W. B.; Huang, D. J.; Liu, Y. W.; Shi, Y. L.; Fang, J. K.; Nie, A. M.; Li, H. Q.; Zhai, T. Y. Engineering a local free water enriched microenvironment for surpassing platinum hydrogen evolution activity. *Angew. Chem., Int. Ed.* **2022**, *61*, e202206077.

[13] Liao, L.; Wang, S. N.; Xiao, J. J.; Bian, X. J.; Zhang, Y. H.; Scanlon, M. D.; Hu, X. L.; Tang, Y.; Liu, B. H.; Girault, H. H. A nanoporous molybdenum carbide nanowire as an electrocatalyst for hydrogen evolution reaction. *Energy Environ. Sci.* **2014**, *7*, 387–392.

[14] Lin, L. L.; Zhou, W.; Gao, R.; Yao, S. Y.; Zhang, X.; Xu, W. Q.; Zheng, S. J.; Jiang, Z.; Yu, Q. L.; Li, Y. W. et al. Low-temperature hydrogen production from water and methanol using Pt/α-MoC catalysts. *Nature* **2017**, *544*, 80–83.

[15] Jia, J.; Xiong, T. L.; Zhao, L. L.; Wang, F. L.; Liu, H.; Hu, R. Z.; Zhou, J.; Zhou, W. J.; Chen, S. W. Ultrathin N-doped Mo_2C nanosheets with exposed active sites as efficient electrocatalyst for hydrogen evolution reactions. *ACS Nano* **2017**, *11*, 12509–12518.

[16] Wu, J. B.; Su, J. W.; Wu, T.; Huang, L.; Li, Q.; Luo, Y. X.; Jin, H. R.; Zhou, J.; Zhai, T. Y.; Wang, D. S. et al. Scalable synthesis of 2D Mo_2C and thickness-dependent hydrogen evolution on its basal plane and edges. *Adv. Mater.* **2023**, *35*, 2209954.

[17] Zhu, C. R.; Gao, D. Q.; Ding, J.; Chao, D. L.; Wang, J. TMD-based highly efficient electrocatalysts developed by combined computational and experimental approaches. *Chem. Soc. Rev.* **2018**, *47*, 4332–4356.

[18] Chen, Z. X.; Leng, K.; Zhao, X. X.; Malkhandi, S.; Tang, W.; Tian, B. B.; Dong, L.; Zheng, L. R.; Lin, M.; Yeo, B. S. et al. Interface confined hydrogen evolution reaction in zero valent metal nanoparticles-intercalated molybdenum disulfide. *Nat. Commun.* **2017**, *8*, 14548.

[19] Chen, L. X.; Chen, Z. W.; Wang, Y.; Yang, C. C.; Jiang, Q. Design of dual-modified MoS_2 with nanoporous Ni and graphene as efficient catalysts for the hydrogen evolution reaction. *ACS Catal.* **2018**, *8*, 8107–8114.

[20] Xie, J. F.; Zhang, H.; Li, S.; Wang, R. X.; Sun, X.; Zhou, M.; Zhou, J. F.; Lou, X. W.; Xie, Y. Defect-rich MoS_2 ultrathin nanosheets with additional active edge sites for enhanced electrocatalytic hydrogen evolution. *Adv. Mater.* **2013**, *25*, 5807–5813.

[21] Lukowski, M. A.; Daniel, A. S.; Meng, F.; Forticaux, A.; Li, L. S.; Jin, S. Enhanced hydrogen evolution catalysis from chemically exfoliated metallic MoS_2 nanosheets. *J. Am. Chem. Soc.* **2013**, *135*, 10274–10277.

[22] Guo, S. E.; Tang, Y. Q.; Xie, Y.; Tian, C. G.; Feng, Q. M.; Zhou, W.; Jiang, B. J. P-doped tubular g-C_3N_4 with surface carbon defects: Universal synthesis and enhanced visible-light photocatalytic hydrogen production. *Appl. Catal. B: Environ.* **2017**, *218*, 664–671.

[23] Jing, S. Y.; Zhang, L. S.; Luo, L.; Lu, J. J.; Yin, S. B.; Shen, P. K.; Tsiakaras, P. N-doped porous molybdenum carbide nanobelts as efficient catalysts for hydrogen evolution reaction. *Appl. Catal. B: Environ.* **2018**, *224*, 533–540.

[24] Liu, W.; Wang, X. T.; Wang, F.; Du, K. F.; Zhang, Z. F.; Guo, Y. Z.; Yin, H. Y.; Wang, D. H. A durable and pH-universal self-standing MoC–Mo_2C heterojunction electrode for efficient hydrogen evolution reaction. *Nat. Commun.* **2021**, *12*, 6776.

[25] Zhang, Y. Z.; Guo, P.; Guo, S. H.; Xin, X.; Wang, Y. J.; Huang, W. J.; Wang, M. H.; Yang, B. W.; Jorge Sobrido, A.; Ghasemi, J. B. et al. Gradient heating epitaxial growth gives well lattice-matched Mo_2C–Mo_2N heterointerfaces that boost both electrocatalytic hydrogen evolution and water vapor splitting. *Angew. Chem., Int. Ed.* **2022**, *61*, e202209703.

[26] Li, H. J. W.; Cai, C.; Wang, Q. Y.; Chen, S. Y.; Fu, J. W.; Liu, B.; Hu, Q. N.; Hu, K. M.; Li, H. M.; Hu, J. H. et al. High-performance alkaline water splitting by Ni nanoparticle-decorated Mo–Ni microrods: Enhanced ion adsorption by the local electric field. *Chem. Eng. J.* **2022**, *435*, 134860.

[27] Gargiulo, J.; Berté, R.; Li, Y.; Maier, S. A.; Cortés, E. From optical to chemical hot spots in plasmonics. *Acc. Chem. Res.* **2019**, *52*, 2525–2535.

[28] Shi, Y.; Wang, J.; Wang, C.; Zhai, T. T.; Bao, W. J.; Xu, J. J.; Xia, X. H.; Chen, H. Y. Hot electron of Au nanorods activates the electrocatalysis of hydrogen evolution on MoS_2 nanosheets. *J. Am. Chem. Soc.* **2015**, *137*, 7365–7370.

[29] Liu, G. G.; Li, P.; Zhao, G. X.; Wang, X.; Kong, J. T.; Liu, H. M.; Zhang, H. B.; Chang, K.; Meng, X. G.; Kako, T. et al. Promoting

active species generation by Plasmon-induced hot-electron excitation for efficient electrocatalytic oxygen evolution. *J. Am. Chem. Soc.* **2016**, *138*, 9128–9136.
[30] Zhang, Z. L.; Zhang, C. Y.; Zheng, H. R.; Xu, H. X. Plasmon-driven catalysis on molecules and nanomaterials. *Acc. Chem. Res.* **2019**, *52*, 2506–2515.
[31] Christopher, P.; Xin, H. L.; Marimuthu, A.; Linic, S. Singular characteristics and unique chemical bond activation mechanisms of photocatalytic reactions on plasmonic nanostructures. *Nat. Mater.* **2012**, *11*, 1044–1050.
[32] Cortés, E. Activating plasmonic chemistry. *Science* **2018**, *362*, 28–29.
[33] Zhao, J.; Xue, S.; Ji, R. R.; Li, B.; Li, J. H. Localized surface Plasmon resonance for enhanced electrocatalysis. *Chem. Soc. Rev.* **2021**, *50*, 12070–12097.
[34] Aslam, U.; Chavez, S.; Linic, S. Controlling energy flow in multimetallic nanostructures for plasmonic catalysis. *Nat. Nanotechnol.* **2017**, *12*, 1000–1005.
[35] Nan, L.; Giráldez-Martínez, J.; Stefancu, A.; Zhu, L.; Liu, M.; Govorov, A. O.; Besteiro, L. V.; Cortés, E. Investigating plasmonic catalysis kinetics on hot-spot engineered nanoantennae. *Nano Lett.* **2023**, *23*, 2883–2889.
[36] Zhou, Y. J.; Liang, Y. Q.; Fu, J. W.; Liu, K.; Chen, Q.; Wang, X. Q.; Li, H. M.; Zhu, L.; Hu, J. H.; Pan, H. et al. Vertical Cu nanoneedle arrays enhance the local electric field promoting C2 hydrocarbons in the CO_2 electroreduction. *Nano Lett.* **2022**, *22*, 1963–1970.
[37] Li, H. J. W.; Zhou, H. M.; Zhou, Y. J.; Hu, J. H.; Miyauchi, M.; Fu, J. W.; Liu, M. Electric-field promoted C–C coupling over Cu nanoneedles for CO_2 electroreduction to C_2 products. *Chin. J. Catal.* **2022**, *43*, 519–525.
[38] Ezendam, S.; Herran, M.; Nan, L.; Gruber, C.; Kang, Y.; Gröbmeyer, F.; Lin, R.; Gargiulo, J.; Sousa-Castillo, A.; Cortés, E. Hybrid plasmonic nanomaterials for hydrogen generation and carbon dioxide reduction. *ACS Energy Lett.* **2022**, *7*, 778–815.
[39] Wang, S. S.; Jiao, L.; Qian, Y. Y.; Hu, W. C.; Xu, G. Y.; Wang, C.; Jiang, H. L. Boosting electrocatalytic hydrogen evolution over metal-organic frameworks by Plasmon-induced hot-electron injection. *Angew. Chem., Int. Ed.* **2019**, *58*, 10713–10717.
[40] Xu, J.; Gu, P.; Birch, D. J. S.; Chen, Y. Plasmon-promoted electrochemical oxygen evolution catalysis from gold decorated MnO_2 nanosheets under green light. *Adv. Funct. Mater.* **2018**, *28*, 1801573.
[41] Liu, C. X.; Gao, C. C.; Yao, K. L.; Masouleh, S. S. M.; Berté, R.; Ren, H. R.; de S. Menezes, L. ; Cortés, E.; Bicket, I. C. et al. Self-constructed multiple plasmonic hotspots on an individual fractal to amplify broadband hot electron generation. *ACS Nano* **2021**, *15*, 10553–10564.
[42] Zhang, Y. F.; Wang, Q. M.; Wang, K. K.; Liu, Y.; Zou, L. W.; Zhou, Y.; Liu, M.; Qiu, X. Q.; Li, W. Z.; Li, J. Plasmonic Ag-decorated Cu_2O nanowires for boosting photoelectrochemical CO_2 reduction to multi-carbon products. *Chem. Commun.* **2022**, *58*, 9421–9424.
[43] Kuo, T. R.; Lee, Y. C.; Chou, H. L.; Swathi, M. G.; Wei, C. Y.; Wen, C. Y.; Chang, Y. H.; Pan, X. Y.; Wang, D. Y. Plasmon-enhanced hydrogen evolution on specific facet of silver nanocrystals. *Chem. Mater.* **2019**, *31*, 3722–3728.
[44] Creel, E. B.; Corson, E. R.; Eichhorn, J.; Kostecki, R.; Urban, J. J.; McCloskey, B. D. Directing selectivity of electrochemical carbon dioxide reduction using plasmonics. *ACS Energy Lett.* **2019**, *4*, 1098–1105.
[45] Chen, X.; Zheng, Z. F.; Ke, X. B.; Jaatinen, E.; Xie, T. F.; Wang, D. J.; Guo, C.; Zhao, J. C.; Zhu, H. Y. Supported silver nanoparticles as photocatalysts under ultraviolet and visible light irradiation. *Green Chem.* **2010**, *12*, 414–419.
[46] Kresse, G.; Furthmüller, J. Efficiency of *ab-initio* total energy calculations for metals and semiconductors using a plane-wave basis set. *Comput. Mater. Sci.* **1996**, *6*, 15–50.
[47] Blöchl, P. E. Projector augmented-wave method. *Phys. Rev. B* **1994**, *50*, 17953–17979.
[48] Ernzerhof, M.; Scuseria, G. E. Assessment of the Perdew–Burke–Ernzerhof exchange-correlation functional. *J. Chem. Phys.* **1999**, *110*, 5029–5036.
[49] Grimme, S.; Antony, J.; Ehrlich, S.; Krieg, H. A consistent and accurate *ab initio* parametrization of density functional dispersion correction (DFT-D) for the 94 elements H–Pu. *J. Chem. Phys.* **2010**, *132*, 154104.
[50] Xu, H. Y.; Zhu, J. Z.; Zou, C. H.; Zhang, F. P.; Ming, D. M.; Guan, D. Q.; Ma, L. Theoretical design of core–shell 3D-metal nanoclusters for efficient hydrogen-evolving reaction. *Energy Fuels* **2023**, *37*, 16781–16789.
[51] Guan, D. Q.; Zhong, J.; Xu, H. Y.; Huang, Y. C.; Hu, Z. W.; Chen, B.; Zhang, Y.; Ni, M.; Xu, X. M.; Zhou, W. et al. A universal chemical-induced tensile strain tuning strategy to boost oxygen-evolving electrocatalysis on perovskite oxides. *Appl. Phys. Rev.* **2022**, *9*, 011422.
[52] Li, W. D.; Xu, H. Y.; Zhang, H. Y.; Wei, F. C.; Huang, L. Y.; Ke, S. Z.; Fu, J. W.; Jing, C. B.; Cheng, J. G.; Liu, S. H. Tuning electron delocalization of hydrogen-bonded organic framework cathode for high-performance zinc-organic batteries. *Nat. Commun.* **2023**, *14*, 5235.
[53] Zhang, C.; Zhou, Y.; Wang, W. J.; Yang, Y.; Zhou, C. Y.; Wang, L. L.; Lei, L.; He, D. H.; Luo, H. Z.; Huang, D. L. Formation of Mo_2C/hollow tubular g-C_3N_4 hybrids with favorable charge transfer channels for excellent visible-light-photocatalytic performance. *Appl. Surf. Sci.* **2020**, *527*, 146757.
[54] Zhou, Y.; Zhang, C.; Huang, D. L.; Wang, W. J.; Zhai, Y. B.; Liang, Q. H.; Yang, Y.; Tian, S. H.; Luo, H. Z.; Qin, D. Y. Structure defined 2D Mo_2C/2D g–C_3N_4 Van der Waals heterojunction: Oriented charge flow in-plane and separation within the interface to collectively promote photocatalytic degradation of pharmaceutical and personal care products. *Appl. Catal. B: Environm.* **2022**, *301*, 120749.
[55] Steinigeweg, D.; Schlücker, S. Monodispersity and size control in the synthesis of 20–100 nm quasi-spherical silver nanoparticles by citrate and ascorbic acid reduction in glycerol-water mixtures. *Chem. Commun.* **2012**, *48*, 8682–8684.